2020 IEEE International Conference on Robotics and Automation (ICRA)
31 May - 31 August, 2020. Paris, France

High Resolution Soft Tactile Interface for Physical Human-Robot Interaction

Isabella Huang[1] and Ruzena Bajcsy[1]

Abstract— **If robots and humans are to coexist and cooperate in society, it would be useful for robots to be able to engage in tactile interactions. Touch is an intuitive communication tool as well as a fundamental method by which we assist each other physically. Tactile abilities are challenging to engineer in robots, since both mechanical safety and sensory intelligence are imperative. Existing work reveals a trade-off between these principles— tactile interfaces that are high in resolution are not easily adapted to human-sized geometries, nor are they generally compliant enough to guarantee safety. On the other hand, soft tactile interfaces deliver intrinsically safe mechanical properties, but their non-linear characteristics render them difficult for use in timely sensing and control. We propose a robotic system that is equipped with a completely soft and therefore safe tactile interface that is large enough to interact with human upper limbs, while producing high resolution tactile sensory readings via depth camera imaging of the soft interface. We present and validate a data-driven model that maps point cloud data to contact forces, and verify its efficacy by demonstrating two real-world applications. In particular, the robot is able to react to a human finger's pokes and change its pose based on the tactile input. In addition, we also demonstrate that the robot can act as an assistive device that dynamically supports and follows a human forearm from underneath.**

I. INTRODUCTION

Physical interaction amongst humans is a natural and essential method by which we communicate with and assist each other. As a communication tool, physical interaction can be more clear and intuitive than providing auditory or visual cues. For example, one can swiftly grab a friend's arm to stop them from walking into incoming traffic, or manually adjust their form when teaching them a new task, such as how to swing a golf club properly. As a means of assistance for those who have limited mobility, physical interaction is even more vital. This is especially clear for caretakers who aid clinical patients or the elderly in everyday tasks such as helping them walk, sit up in bed, or change their clothes.

If robots are to coexist with and be useful to humans, endowing them with similar capabilities of physical interaction would be hugely advantageous and would facilitate a myriad of exciting applications with considerable societal impact. A necessary component of such a robot capable of physical interaction is a tactile interface, which should not only ensure a human's safety during interaction, but also enable the correct sensing of interaction forces. In this work, we propose a tactile interface that strives to address these two concerns of *safety* and *accurate sensing*.

*This work was supported by NSF Award #1545126

[1]The authors are with the Department of Electrical Engineering and Computer Sciences, University of California, Berkeley, CA 94270, USA {isabella.huang, bajcsy}@eecs.berkeley.edu

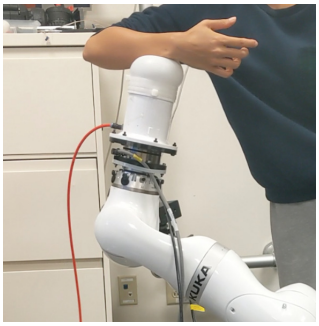

Fig. 1: The proposed soft interface enables safe and precise tactile interaction between a human and a robot.

Our tactile interface consists of a pneumatically pressurized domed contact membrane molded from silicone. The compliant properties of this soft device make it inherently safe for physical interaction with humans. Moreover, our design belongs to an up-and-coming class of optical tactile sensors that utilizes embedded depth-sensing cameras to extract interaction information from a soft contact region. This type of camera offers a richness in visual data that is unmatched by traditional 2D cameras and ultimately enables high sensing accuracy. Specifically, there are two main goals that are desired in tactile sensing. Firstly, it is useful to infer the physical geometry of the object in contact, and it has been shown in our previous work that our design does so extremely efficiently [1]. Secondly, a more difficult goal is to infer the force that is being applied on the sensor. It is not possible to directly read force from vision, so some sort of mapping is required. This is challenging even for a sensor like ours that outputs a high-fidelity 3D membrane representation, as non-linear constituent elastic stress-strain equations require finite element methods that are computationally intensive and highly sensitive to manufacturing parameters. In this work, following the recent successes in the field, data-driven techniques will be employed in the modeling of the soft contact region.

The space of all contact interactions and resultant forces for which to build this mapping is extremely vast, but will be constrained in this work based on two proposed physical human-robot interaction (pHRI) applications that both involve interaction with the human upper limb. These applications are inspired by our motivating examples for physical interaction to be used in *communication* as well as in *assistance*. To demonstrate tactile communication, we show that a human can successfully alter a robot's end effector

pose by indenting the tactile interface in the appropriate location with their fingertip. To exemplify an assistive task, we demonstrate that our soft interface can act as a soft forearm support that adapts to and follows the human's dynamic forearm motions by interpreting the shear and torque forces applied by the human forearm to the tactile interface.

II. RELATED WORKS

A. Design of Tactile Sensors for pHRI

The objective of tactile sensing is to physically interact with the external environment and extract knowledge about it by interpreting salient signals. To this end, many existing soft tactile sensing designs in the past have relied on embedding photoreflective, piezoelectric [2], strain-sensitive [3], electromagnetic [4], and other electronic modules [5] within a compliant material. Such designs are easily arranged into a flat skin-like configuration that then covers a robot body to enable tactile sensing capabilities for interaction with humans or the environment. One main advantage of such skins is that the spatial resolution can be made to be as fine as around the millimeter scale, depending on the engineered density of sensing elements [6]. However, these constituent sensors limit the material strain and compliance that make soft sensors desirable [7]. Moreover, even if the skin itself is soft, overlaying it on top of a hard robot chassis severely limits the achievable compliance during interaction, which poses a safety threat when humans are involved.

Since high-compliance interaction is of the utmost importance for safety, in this work we do not improve traditional tactile skins further, but rather develop a new design for a soft robot end effector interface. An example of existing work based on a similar design goal is the development of a pair of pneumatically pressurized fingers that can carefully pick up fragile objects by sensing an overall pressure change in the fingers upon contact [8]. However, this sensory information is low in resolution, and can neither sense the objects' shapes nor even localize the point of contact. Recently, the leading technique in tactile sensing that does not require embedded sensing elements is optical tactile sensing, in which devices image visual cues from a deformed compliant membrane to reconstruct the interaction effects between the environment and the sensor. Some well-known examples of soft optical tactile sensing devices are the TacTip sensors, which image the distortion of internal papillae of a soft gel-filled membrane, as well as the extremely high-resolution MIT GelSight sensor, which makes use of the superposition of different colored light waves in a gel medium to infer contact information [9]. On the other hand, the optical tactile sensor proposed in our prior work is a high-resolution sensor that directly images the contact membrane via depth camera without needing to reconstruct papillae positions or process color changes. Moreover, its stiffness can be altered pneumatically, which can advantageously modulate different interaction impedances [10]. Furthermore, its simple design is easy to manufacture and extremely scalable. While the lower bound on its geometry is restricted by the range of state-of-the-art depth camera technology and thus renders our design ineffective for very fine manipulation tasks, its larger geometry actually makes it well suited for human-level interaction. Thus, our final design aims to collect the features across tactile sensors that are best suited towards pHRI— high resolution, intrinsic softness, variable stiffness, and appropriate geometric scale.

B. Methods for Inferring Interaction Forces Visually

It is challenging to interpret forces from visual data provided by optical tactile sensing methods. To this end, finite element modeling techniques have been applied to generate a mapping between visual data and contact forces, but this approach is computationally heavy and not suitable for real time control [11]. In the recent years, data-driven methods have proven themselves to be fast and accurate for use with modeling optical tactile sensors. Within the TacTip family, deep learning enabled the fast development of edge detection and contour following capabilities. For even more fine tasks, for example, the GelSight has been a successful platform for learning physical models to detect object hardness [12], or to perform complicated manipulation tasks via reinforcement learning [13], or even to detect differences in fabric texture [14]. As a result of these successes, convolutional neural networks for processing visual data in tactile sensing has become a promising method in the community. In this work, we adopt a similar architecture when creating our own model.

C. Existing Applications in pHRI

The space of existing pHRI applications in general is limited with respect to purpose and precision. In rigid robots, force-torque sensors are the primary transducers for pHRI, enabling interactions for example with robot arms [15] and full-bodied partner ballroom dancing robots [16]. The sensory capabilities of these robots are very powerful, but their pHRI applications are limited due to risk of unsafe interactions with the hard chassis. The scope of existing soft pHRI robots is unsurprisingly even more narrow due to challenging constraints in mechanical design and sensing. Some noteworthy examples of existing soft pHRI systems include RI-MAN, a humanoid robot designed to help lift and carry humans [17], and Huggable, a soft robot pet surrogate [18] that responds to affective touch-based interactions. There is an apparent need in the field to develop robots that can perform useful and precise pHRI task while remaining compliant enough to assure human safety. Thus, this work presents two useful applications of the proposed robotic system that involve completely soft interactions and do not require bulky transducers apart from a small internally embedded camera.

III. DESIGN OF SYSTEM

The system is composed of a soft tactile interface mounted onto the end of a lightweight LBR iiwa 14 R820 robot arm from KUKA AG with its constituent components labeled in Fig. 2. In order to access ground truth force-torque

readings to train the data-driven models, an ATI Axia 6-dof transducer is mounted between the end of the robot arm and the tactile sensing module. The tactile sensor consists of a hemispherical membrane that acts as the tactile interface sealed over a pneumatically-pressurized rigid cylindrical capsule 3D printed from PLA polyester. Though this particular capsule is rigid, it could be shielded with compliant material, or better yet, replaced entirely with a soft structure. Inside the capsule is an embedded Camboard pico flexx time-of-flight depth camera from PMD Technologies, the smallest commercially available depth camera available, which images the membrane internally. The longitudinal distance from the camera to the base of the membrane is 10 cm, which is the camera's lowest nominal range for which a depth image can be resolved correctly. The membrane, molded from Ecoflex^{TM} 50 silicone, has an outer and inner diameter of 100 and 94 mm respectively with a uniform thickness of 3 mm. A 30 mm-long skirt extending from the hemisphere's base allows the silicone membrane to be securely fastened to the cylinder, with three external cable ties tightly enforcing a hermetic seal. The cylinder surface is fully covered with a coat of XTC-3D®resin to prevent air leakage, and the interior of the cylinder is painted with a matte black acrylic paint to absorb any stray reflected rays from the camera laser that lead to distorted camera readings. Ports on the cylinder that allow for the connection of the pico flexx USB cable as well as the pneunatic tubing are also sealed with the resin and additional modeling clay where necessary. An air compressor enables the modulation of pressure state inside the sensor. Since the tactile membrane is designed to be thin so that it would be sensitive enough to contact-induced deformations, it inflates slightly upon internal pressurization. Thus, each internal pressure state is linked to a certain amount of inflation. In this work, all development was performed for one fixed pressure state, particularly the one at which the membrane's inner radius was inflated to 50 mm, compared to its neutral 47 mm radius when free air exchange between the capsule and the atmosphere is permitted. All sensing and actuation is connected to Robot Operating System (ROS) nodes. Since the KUKA robot does not have native ROS support, an open source ROS stack is used to control the KUKA's joint positions [19] and the TRAC-IK library is used for computing inverse kinematics [20].

IV. ADMISSIBLE INTERACTIONS

The space of admissible interactions studied in this work was limited by design based on the two different pHRI applications we wished to achieve. Both applications involve specific interactions with the human upper limb, and illustrate the usage of physical interaction as a means of human-robot *communication* and *assistance* respectively.

A. Robot End Effector Pose Correction

The first application utilizes the tactile interface as a communication tool from the human to the robot. In this regime, the human physically corrects the end effector pose of the robot by prodding the robot towards the desired configuration through interaction with the tactile interface. Here, interactions for this application are limited to single finger poking so that the contact geometry can be kept simple. Thus, we avoid more complicated interactions such as those from multiple fingers and/or the palm.

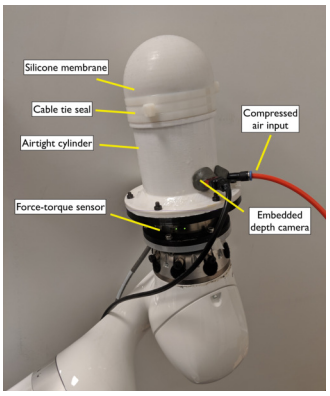

Fig. 2: Components of the composite soft tactile end effector interface.

B. Dynamic Support of the Human Forearm.

The second application enables the robot to act as an assistive device for the human. Specifically, it assists with upper limb motion, a common feature in ergonomic design and exoskeletons that helps minimize the effort required to support the weight of one's arm [21]. In this application, the human's forearm rests on top of and is fully supported by the soft tactile interface. However, such a support system is only useful if the human has autonomy over their own movements. Thus, the device follows and dynamically supports the forearm as it translates in space, as well as rotates with it when a torque about the sensor axis is applied.

V. DATA COLLECTION

Both applications can only be implemented if the robot is aware of the forces and torques being applied to it during interaction. In its most useful form, the robot should only have access to the depth camera readings, since being outfitted with a force-torque sensor renders the overall system less compliant. Thus, mappings that predict the force-torque responsible for a measured membrane point cloud need to be available to the robot. To this end, we systematically collect a dataset of admissible interactions and their resulting induced force, torque, and point clouds in order to train a data-driven model that provides this mapping. There were two datasets, one for each application, that were collected. Note that the coordinate system is defined to be fixed to the ATI force-torque sensor. The principal camera axes also share the same orientation as the force-torque coordinate frame.

A. Finger Poking Dataset

Fingertip apparatus. A rigid sphere 1 cm in diameter printed from PLA was used in the data collecting experiments as an approximate duplicate of an average human fingertip. Since minimal slip and shear was expected for the

poking interactions, it was reasonable to neglect the frictional effects of skin versus PLA.

Pre-indentation contact points. The sphere was then used to indent the membrane at a variety of locations at different angles and depths, and the resultant membrane point cloud and force-torque measurements at each state were recorded. The interaction states were discretized systematically. First, a set of initial contact points on the membrane surface were selected. As illustrated in Fig. 3, this was achieved by designating 40 equally spaced quarter-circle arcs that run from the pole to the base of the hemisphere (parameterized by $\phi = \frac{\pi j}{20}, j \in [0..39]$). Along each quarter-circle arc, five points were selected with projections on the xy-plane that are equally spaced with radii 0 to 4 cm from the pole, leaving enough of a distance from the base of the hemisphere so that boundary contact conditions could be avoided. These initial contact points indicate the location at which the spherical obstacle first makes contact with the membrane to begin indentation.

Indentation locations Then, the sphere indented the membrane at varying depths and angles from the z-axis. As illustrated in Fig. 4, each pre-indentation contact point was the starting point for 10 different indentation directions ($\theta = \frac{\pi k}{18}, k \in [0..9]$). Along each indentation direction, five different indentation depths δ equally spaced from 0.5 to 2.5 cm were visited. All indentation locations that stemmed from any one pre-indentation contact point were constrained to one plane, and interactions were actuated by the KUKA arm pushing into the fixed sphere at the appropriate angles and depths. In total, there were 10,000 unique states for which data was collected.

Visualization of example data. Figs. 5a, 5d, and 5g are radial plots of ground truth τ_x at a particular indentation state parameterized by θ and δ starting from every pre-indentation contact state, where the size of each marker is scaled according to the magnitude of τ_x. Between Figs. 5a and 5d, the magnitude of the measured τ_x is greater in 5d, due to its indentation depth being 1 cm deeper. Fig. 5g depicts the torque value when the θ is large enough that torque applied is in the opposite direction compared to a smaller θ such as in Fig. 5d. The magnitude is also larger because the moment arm to the x-axis attached to the force-torque sensor becomes longer.

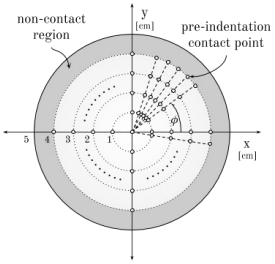

Fig. 3: Polar view of the pre-indentation fingertip contact points that lie on 40 evenly-spaced quarter-circle arcs.

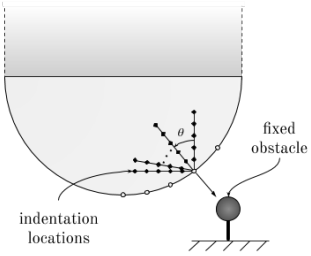

Fig. 4: Side view of the pre-indentation contact points and the indentation locations associated with each.

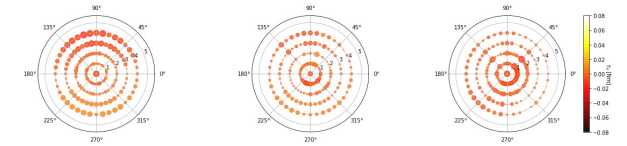

(a) $\theta = \frac{\pi}{18}$ rad, $\delta =$ 1.5 cm (b) $\theta = \frac{\pi}{18}$ rad, $\delta =$ 1.5 cm (c) $\theta = \frac{\pi}{18}$ rad, $\delta =$ 1.5 cm

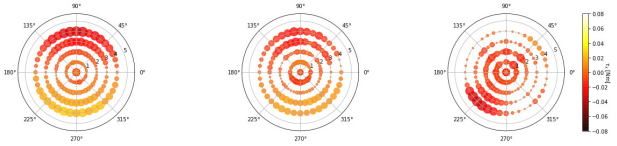

(d) $\theta = \frac{\pi}{18}$ rad, $\delta =$ 2.5 cm (e) $\theta = \frac{\pi}{18}$ rad, $\delta =$ 2.5 cm (f) $\theta = \frac{\pi}{18}$ rad, $\delta =$ 2.5 cm

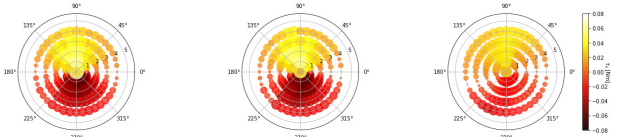

(g) $\theta = \frac{7\pi}{18}$ rad, $\delta =$ 2.5 cm (h) $\theta = \frac{7\pi}{18}$ rad, $\delta =$ 2.5 cm (i) $\theta = \frac{7\pi}{18}$ rad, $\delta =$ 2.5 cm

Fig. 5: Polar plot of τ_x in the fingertip dataset starting at all pre-indentation contact points for selected values of θ and δ. Columns separate ground truth readings (left), prediction learned from poking data (middle), and prediction learned from both poking and forearm data (right).

B. Forearm Shearing and Torquing Dataset

Forearm apparatus. An attempt to replicate a generic forearm geometry using a simple 3D-printed ellipsoid was unsuccessful due to the different material properties between PLA and human skin yielding different frictional forces during interaction. Thus, data was collected using the researcher's real forearm. The forearm was placed directly underneath the sensor during data collection such that its axis was centered on the membrane. A fixed brace was used to keep the forearm consistently in the same place between data collection sessions.

Shearing. The device pushed into the forearm until an indentation depth δ was achieved, as measured from the z-displacement of the pole. Fig. 6 illustrates the indentation locations visited by the forearm contact point. Then, the device moved in a specific direction parameterized by ϕ in the xy-plane, defined in the same way as in Fig. 3 of the fingertip experiment, and stopped at 5 different distances from 0.3 to 1.5 cm away. This shearing distance was limited to avoid material slip. This process was then repeated for $\phi = \frac{2\pi l}{40}, l \in [0..40]$ rad and also for $\delta = \frac{m}{4}, m \in [0..8]$ cm.

Torquing. In the same manner as the shearing experiments, the device pushed into the forearm until an indentation depth δ was achieved. Then, the device rotated about its z-axis in one direction, stopping at angles $\psi = \frac{\pi n}{24}, n \in [0..8]$. for data recording. The maximum rotation angle achieved, $\frac{\pi}{3}$, was limited to avoid material slip from excessive torquing.

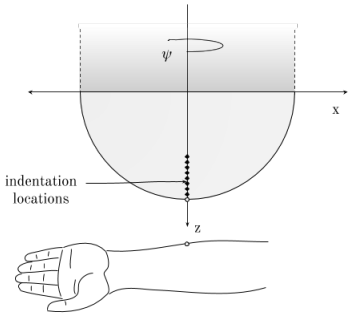

Fig. 6: Side view of the forearm indentation states. Arm is not drawn to scale.

This was repeated for rotation in the opposite direction, and then also for $\delta = \frac{p}{4}, p \in [0..8]$ cm. For both the shearing and torquing motions, data was collected for 1726 interaction states. In order to achieve a better distribution of samples, the forearm experiments were repeated 4 more times so that a total of 8640 datapoints were collected.

VI. FORCE-DEFORMATION MODEL

A. Architecture

The neural network architecture used to map the input of a 171×224 organized point cloud into a 6-dimensional force-torque vector is illustrated in Fig. 9. Each point cloud input, an array of depth measurements, is passed through a series of two convolutional and max-pooling layers, and then through a fully-connected regression network to yield the predicted resultant force-torque measurement. We trained three different models with the same architecture. The first model combined the data from the two datasets, and the other two were trained on either just the poking or the forearm dataset. Since the two interaction regimes are quite different, we wanted to explore whether the combined dataset network would be able to generalize and perform as well as each of the individial dataset models. The networks were trained with the SGD optimizer and a learning rate of 0.01 with no decay, and a dropout of 0.2 was implemented in the fully-connected layers to prevent overfitting. An 80:20 train/test split was selected for hyperparameter tuning and validation. The finger poking dataset, with 10,000 total datapoints, leveled out to

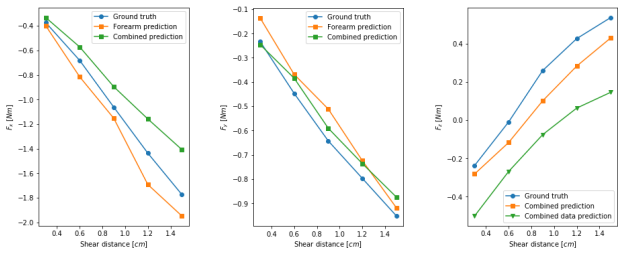

(a) Predicted F_x (b) Predicted F_y (c) Predicted F_z

Fig. 7: Forearm shearing example validation data at $\phi = 3\pi 4$ and $\delta = 0.75$ cm comparing the predictions of the forearm and combined models with the ground truth.

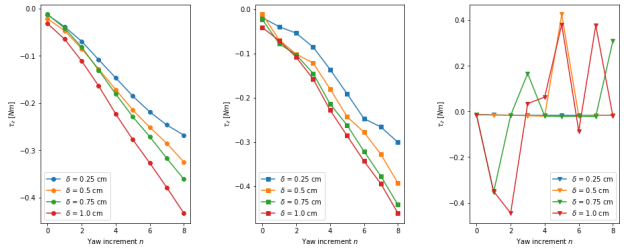

(a) Ground truth data. (b) Forearm model prediction. (c) Combined model prediction.

Fig. 8: Predicted τ_z on example forearm torquing validation data as a function of the yaw angle for different indentation depths δ.

a validation MSE of 0.03 after training with a batch size of 500. The forearm dataset, with a total of 8640 datapoints, yielded a final validation MSE of 0.057 after training with a batch size of 400. The combined dataset yielded a final validation MSE of 0.1 with a training batch size of 500. All force-torque values were recorded in SI units.

B. Prediction Results

We found that in general, the two models trained on the individual datasets performed very well in validation. For example, in Fig. 5 we can compare the performance of the poking dataset model (middle columm) with the ground truth (left column) and note that the prediction is qualitatively accurate. However, it is apparent that the combined model (right column) yields less accurate predictions, which can be vastly different from the ground truth. For example, in Fig. 5f, the sign on the τ_x reading in the third quadrant is evidently wrong. The performance of the forearm model was also very good in predicting forearm shear and torquing forces. Fig. 7 visualizes example validation data for both the forearm and the combined models on a set of ground truth forearm shearing readings at $\phi = \frac{3\pi}{4}$ at a depth of $\delta = 0.75$ cm. Qualitatively, both models perform well. However, when predicting forearm torques, with example prediction on validation data in Fig. 8, the combined model fails to output good prediction. One explanation is that while shearing and poking interactions involve pushing, the twisting involved in torquing yields more complicated membrane structures, and there was not enough training data for the combined model to generalize well.

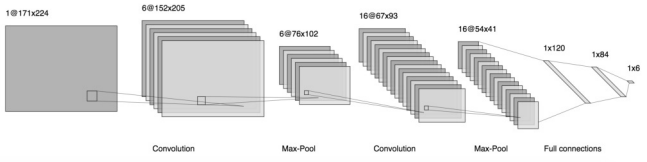

Fig. 9: Architecture of the force-torque-deformation model.

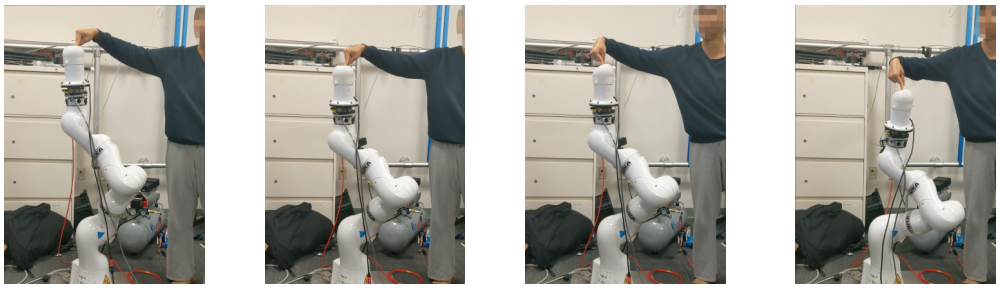

(a) User uses their finger to poke along and opposite to the z-axis of the robot.

(b) Robot changes position proportional to its sensed contact force.

(c) User pokes at the interface at an angle to the z-axis.

(d) Robot changes position and orientation according to the user's force-torque input.

Fig. 10: Real-world validation of the robot end effector pose correction application.

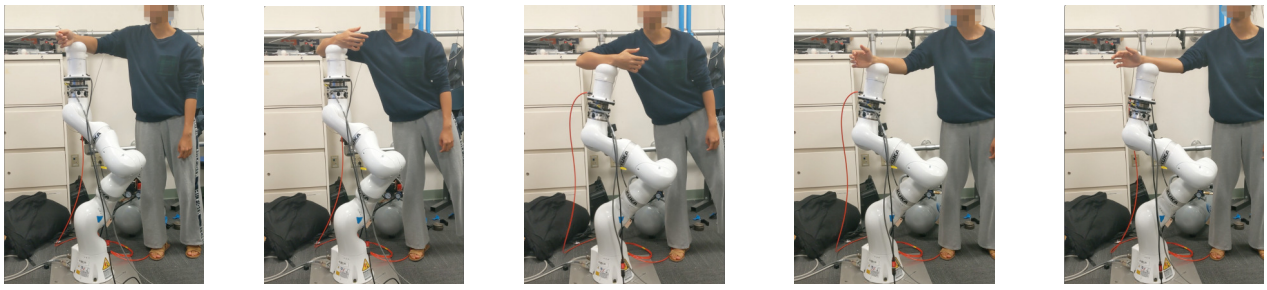

(a) User begins by resting their forearm on the soft interface.

(b) User applies a combined shear and torsional force to the robot.

(c) Robot reacts by changing both its position and orientation.

(d) User attempts to exert a pure torque on the interface.

(e) Robot reacts by twisting in the same direction as the applied torque.

Fig. 11: Real world validation of the dynamic forearm support.

VII. REAL-WORLD RESULTS

We perform a proof-of-concept demonstration of the two applications in which the robot uses its learned force-deformation models. For each application, we utilize the individually trained models rather than the combined one due to their higher accuracy. Example snapshots are depicted in Figs. 10 and 11. For the two cases, we implement the same simple control loop at a slow 1 Hz rate for safety purposes, at which the robot changes its configuration based on its the predicted force and torque from the point cloud stream. At each update step, where values are measured in SI units, the robot position in the world frame $p = [p_x \ p_y \ p_z]^T$ is updated according to $p_i \leftarrow p_i + 0.1F_i, i \in \{x, y, z\}$. Additionally, a rotation about each of the principal axes in the body frame attached to the base of the cylinder (ie. at the force sensor), is applied according to $R_i(2\tau_i)$ where R_i is the rotation operator about the i^{th} principal axis. These constants were chosen empirically such that they yield a large enough change in robot joint configuration at each step without being too sensitive to sensor noise. In the forearm application, the force is initially zeroed at the resting position (ie. when the forearm's weight is fully supported by the robot). As expected from the good validation results in the models, the system was reliable and consistently responded as expected. However, an in-depth user study was not performed, so the usability and comfort of the system is not confirmed here.

VIII. LIMITATIONS AND FUTURE WORK

We have presented a promising new design for a tactile interface in pHRI applications with a learned model mapping point cloud measurements to contact forces and torques. We validated the model with two real-world applications motivated by relevant challenges in pHRI today. However, our work is limited in many ways. Firstly, the generalizability of the learned force-deformation model is nowhere near what can be attained using physical constituent relations. As evident from the combined model performing unreliably compared to the individually trained models, a much broader set of interactions must be collected if pure data-driven techniques are to be employed. An imminent goal for future work is to develop a model-based framework that leverages known physical relationships in elastic shell theory. This would enable more complicated interactions with the interface such as those with different parts of the upper limb or complex multifingered interactions such as pinching. For instance, our current system would not even be able to react to forces directed away from the camera. Though not explored here, physics-based models should also help generalize performance across different human users with different limb sizes. Moreover, running the system at a higher control rate would be more compelling for real world applications, and it would be way to test and develop real-time HRI algorithms for human-robot teaming and teaching.

REFERENCES

[1] R. Bajcsy I. Huang J. Liu. "A Depth Camera-Based Soft Fingertip Device for Contact RegionEstimation and Perception-Action Coupling". In: *2019 International Conference on Robotics and Automation (ICRA)*. 2019.

[2] J. Dargahi. "A three sensing element piezoelectric tactile sensor for robotic and prosthetic applications". In: *Sensors and Actuators A-physical* 80 (2000), pp. 23–30.

[3] Jonathan Engel, Jack Chen, and Chang Liu. "Development of polyimide flexible tactile sensor skin". In: *J. Micromech. Microeng* 13 (May 2003), pp. 359–366.

[4] S. Takenawa. "A soft three-axis tactile sensor based on electromagnetic induction". In: *2009 IEEE International Conference on Mechatronics*. 2009, pp. 1–6.

[5] N. Lu and D.H. Kim. "Flexible and Stretchable Electronics Paving the Way for Soft Robotics". In: *Soft Robotics* 1.1 (2014), pp. 53–62.

[6] Brenna D. Argall and Aude G. Billard. "A survey of Tactile Human-Robot Interactions". In: *Robotics and Autonomous Systems* 58.10 (2010), pp. 1159–1176. ISSN: 0921-8890.

[7] R.S. Fearing. "Tactile Sensing Mechanisms". In: *The International Journal of Robotics Research* 9.3 (1990), pp. 3–23.

[8] Joohyung Kim, Alexander Alspach, and Katsu Yamane. "3D printed soft skin for safe human-robot interaction". In: Sept. 2015, pp. 2419–2425.

[9] R. Li et al. "Localization and manipulation of small parts using GelSight tactile sensing". In: *2014 IEEE/RSJ International Conference on Intelligent Robots and Systems*. 2014, pp. 3988–3993.

[10] Giovanni Tonietti, R. Schiavi, and Antonio Bicchi. "Design and Control of a Variable Stiffness Actuator for Safe and Fast Physical Human/Robot Interaction". In: May 2005, pp. 526–531. ISBN: 0-7803-8914-X.

[11] Thomas H. Speeter. "Three-dimensional Finite Element Analysis of Elastic Continua for Tactile Sensing". In: *The International Journal of Robotics Research* 11.1 (1992), pp. 1–19.

[12] W. Yuan et al. "Shape-independent hardness estimation using deep learning and a GelSight tactile sensor". In: *2017 IEEE International Conference on Robotics and Automation (ICRA)*. May 2017, pp. 951–958.

[13] A. Gupta et al. "Learning dexterous manipulation for a soft robotic hand from human demonstrations". In: *2016 IEEE/RSJ International Conference on Intelligent Robots and Systems (IROS)*. Oct. 2016, pp. 3786–3793.

[14] Rui Li and Edward H. Adelson. "Sensing and Recognizing Surface Textures Using a GelSight Sensor". In: *The IEEE Conference on Computer Vision and Pattern Recognition (CVPR)*. June 2013.

[15] Andrea Bajcsy et al. "Learning robot objectives from physical human interaction". In: Nov. 2017.

[16] K. Kosuge et al. "Dance partner robot - Ms DanceR". In: *Proceedings 2003 IEEE/RSJ International Conference on Intelligent Robots and Systems (IROS 2003) (Cat. No.03CH37453)*. Vol. 4. Oct. 2003, 3459–3464 vol.3.

[17] T. Mukai et al. "Development of the Tactile Sensor System of a Human-Interactive Robot "RI-MAN"". In: *IEEE Transactions on Robotics* 24.2 (Apr. 2008), pp. 505–512.

[18] W.D. Stiehl et al. "The design of the huggable: A therapeutic robotic companion for relational, affective touch". In: vol. 2005. Sept. 2005, pp. 408–415. ISBN: 0-7803-9274-4.

[19] Christoph Hennersperger et al. "Towards MRI-based autonomous robotic US acquisitions: a first feasibility study". In: *IEEE transactions on medical imaging* 36.2 (2017), pp. 538–548.

[20] P. Beeson and B. Ames. "TRAC-IK: An open-source library for improved solving of generic inverse kinematics". In: *2015 IEEE-RAS 15th International Conference on Humanoid Robots (Humanoids)*. Nov. 2015, pp. 928–935.

[21] Mohammad Rahman et al. "Development and Control of a Robotic Exoskeleton for Shoulder, Elbow and Forearm Movement Assistance". In: *Applied Bionics and Biomechanics* 9 (July 2012), pp. 275–292.